A Rich Spectrum of Neural Field Dynamics in the Presence of Short-Term Synaptic Depression

He Wang,[1] Kin Lam,[1] C. C. Alan Fung,[1] K. Y. Michael Wong,[1] and Si Wu[2]

[1] *Department of Physics, Hong Kong University of Science and Technology, Hong Kong, China*
[2] *State Key Laboratory of Cognitive Neuroscience and Learning, IDG/McGovern Institute for Brain Research, Beijing Normal University, Beijing 100875, China*

(Dated: February 13, 2015)

In continuous attractor neural networks (CANNs), spatially continuous information such as orientation, head direction, and spatial location is represented by Gaussian-like tuning curves that can be displaced continuously in the space of the preferred stimuli of the neurons. We investigate how short-term synaptic depression (STD) can reshape the intrinsic dynamics of the CANN model and its responses to a single static input. In particular, CANNs with STD can support various complex firing patterns and chaotic behaviors. These chaotic behaviors have the potential to encode various stimuli in the neuronal system.

PACS numbers: 87.85.dq,05.45.-a, 87.19.ll

arXiv:1502.03662v1 [q-bio.NC] 12 Feb 2015

I. INTRODUCTION

To understand the brain's operation, it is important to consider the range of firing patterns and their conditions of occurrence, which will shed light on how information is encoded in the brain [1]. In the processing of continuous information such as object orientation and spatial location, firing patterns are found to be localized in the space of preferred stimuli of the neurons, normally taking up a Gaussian-like profile [2, 3]. Thus an interesting question is whether these profiles are stable in time and in space and, if not, what other dynamical states will replace them.

Gaussian-like profiles play an important role in both experiments and theory. The tuning curves, i.e., the functional dependence of the neuronal response on the inputs and the preferred stimuli of the neurons, are observed as Gaussian-like profiles in various animal experiments. For example, head direction cells in anterior thalamus and postsubiculum were found in rodents [4–6]. Their tuning curves are Gaussian-like and centered at their preferred head directions. Place cells in hippocampus are another example [7, 8]. Place cells' activities are observed to depend on the location of the animal within the environment. The tuning curve is also a Gaussian-like function. Moving direction cells in middle temporal (MT or V5) cortex in macaques are found to be selective to object moving directions, which also have Gaussian-like tuning curves [9, 10].

In neural field models processing continuous information, Gaussian-like tuning curves are steady states of the network dynamics, and remain stable when their positions are displaced in the space of the preferred stimuli of the neurons. These neural field models are called continuous attractor neural networks (CANNs), since the Gaussian-like tuning curves are attractors of the network dynamics. Recent evidence supporting the existence of continuous attractors was reported by Wimmer *et al.*, who discovered activity anticorrelations on the opposite sides of tuning curves as predicted by the CANN model in the prefrontal cortex of monkeys [11–13].

The ability to support these bump attractors is effected by couplings between neurons in CANNs. However, in reality, couplings between neurons are not quenched. They depend on firing histories of presynaptic neurons. Tsodyks *et al.* found that synaptic efficacy decreases with firing history [14, 15]. Furthermore, they proposed that this decline in synaptic efficacy is due to the slow dynamics of the recovery process of neurotransmitters. The recovery of neurotransmitters is of the order of 100 ms. This short-term decline in synaptic efficacy is called short-term synaptic depression (STD).

Various effects of STD on CANN have been studied in the literature. For instance, Fung *et al.* reported that CANN with STD can support four different phases according to strengths of inhibition and STD [16]. In particular, STD can drive traveling bumps in the attractor space (see Fig. 1(c)). These moving profiles happen in the absence of external inputs. Additionally, York and van Rossum reported a similar result, but with a uniform background current [17].

Moreover, the network's response can be modulated by the interplay between the STD-driven intrinsic dynamics and a moving stimulus. Without STD, a bump-shaped neuronal activity profile tracks a moving stimulus with a delay. However, with a proper strength of STD, the network activity profile can move ahead of the moving stimulus. Effectively, the network activity profile is located at a future position of the moving stimulus. It can be used to implement an anticipation mechanism, which can compensate inherent delays in the neural system, thus achieving real-time tracking [18].

For a static input, short-term synaptic depression can also drive periodic excitements of neuronal activity [19]. We proposed that these periodic excitements enable CANNs to support representations of multiple stimuli almost simultaneously [20]. These periodic excitements provide a plausible mechanism for resolution enhancement in transparent motion [10, 21].

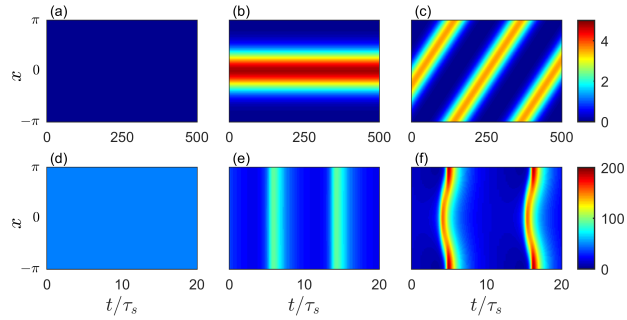

FIG. 1. (Color online) Intrinsic Behaviors. The color scale shows $U(x,t)$. (a) Silent state. Parameters: $k = 0.8$, $\beta = 0.2$. (b) Static bump. Parameters: $k = 0.8$, $\beta = 0.005$. (c) Moving bump. Parameters: $k = 0.8$, $\beta = 0.05$. (d) Uniform firing. Parameters: $k = 1\times10^{-4}$, $\beta = 0.02$. (e) Homogeneous spikes. Parameters: $k = 1\times10^{-4}$, $\beta = 0.023$. (f) Spikes and anti-spikes. Parameters: $k = 1\times10^{-4}$, $\beta = 0.0245$. For all (a)-(f), $a = 0.6$.

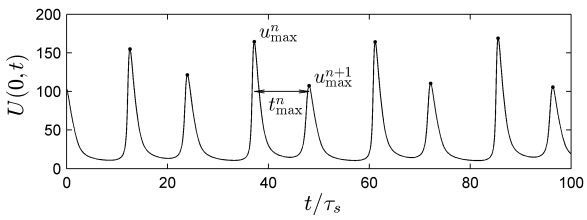

FIG. 2. Chaotic Spikes. The trajectory of $U(0,t)$. Parameters: $k = 3.7\times10^{-4}$, $\beta = 0.026999$, and $a = 0.6$.

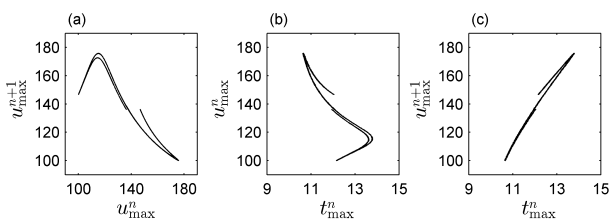

FIG. 3. Lorenz maps of chaotic spikes. (a) The relation between $u^{n+1}_{\max}$ and $u^n_{\max}$. (b) The relation between $t^n_{\max}$ and $u^n_{\max}$. (c) The relation between $t^n_{\max}$ and $u^{n+1}_{\max}$. Simulation runs for $50000\tau_s$. Parameters are the same as in Fig. 2.

The above examples indicate that in the presence of STD, the dynamics of CANNs has a rich spectrum. The intrinsic dynamics is further enriched in response to external stimuli. So, it is important to systematically study the structure of the dynamics of CANNs with STD. In this paper, we report our investigations of CANN with STD in two scenarios: one with very weak inhibition and the other with moderate inhibition in the presence of a single static input.

For CANNs with STD and very weak inhibition, the dynamical picture is more complicated than that with moderate inhibition strengths, which only consists of phases with static bumps, metastatic bumps, moving bumps, and the silent state [16]. Depending on parameters, the system can support the following behaviors: uniform firing patterns across the whole network, periodic excitements of uniform firing, wave instabilities with complex and even chaotic firing patterns.

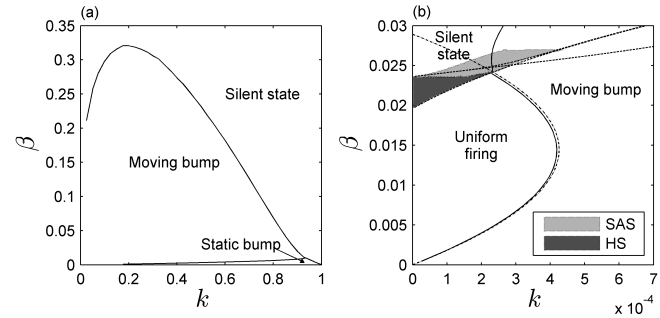

FIG. 4. Phase diagram of CANN with STD. (a) Moderate global inhibition. (b) Weak global inhibition. Moving bump exists on the right side of the solid line. Light gray area (SAS) is for spikes and anti-spikes. Dark gray area (HS) is for homogeneous spikes. Dashed lines are boundaries of the simplified dynamics (Eqs. (8) and (9)). They are discussed in region B in Fig. 6. The dot-dashed line is the boundary between the uniform firing state and the moving bump state given by Eq. (16).

For CANNs with STD and a single static input, the network can support various complex firing patterns. Those complex patterns are due to the interplay between the STD-driven intrinsic dynamics and the external input, depending on strengths of the single static input, inhibition and STD. Similar to the previous scenario, some complex patterns are chaotic.

The rest of the paper is organized as follows. We will begin with an introduction of the model being used throughout the paper. Next, we will present the intrinsic dynamics of the CANN with STD and very weak inhibition. After that, we will report how the dynamics of the system is affected by the external input. Detailed behaviors of the network in various phases in the phase diagram will also be reported. The relevance of the results will be discussed at the end.

II. INTRINSIC BEHAVIORS UNDER WEAK GLOBAL INHIBITION

N neurons are evenly distributed in the space of preferred stimuli (in the following simulation results, $N = 256$). Neurons are labeled by their preferred stimulus x. The range of $\{x\}$ is $(-L/2, L/2]$. So the size of the space is L. Since usually the model is applied to the representation of directions or orientations, $L = 2\pi$ and the periodic boundary condition is imposed. We modify the general form of neural field theory and formulate the intrinsic dynamics of the neuronal input $\widetilde{U}(x,t)$ as

[2, 16, 22, 23]

$$\tau_s \frac{\partial \widetilde{U}(x,t)}{\partial t} = \rho \int_{-L/2}^{L/2} dx' J(x,x') p(x',t) \widetilde{r}(x',t) - \widetilde{U}(x,t) + \widetilde{I}(x,t), \quad (1)$$

where ρ is the density of neurons in the space of preferred stimuli, $\widetilde{I}(x,t)$ is the external stimulus, $J(x,x')$ is the coupling strength between neurons with preferred stimuli x and x', $\widetilde{r}(x',t)$ is the firing rate of neuron x' at time t. They are given by

$$J(x,x') = \frac{J_0}{\sqrt{2\pi}a} \exp\left[-\frac{(x-x')^2}{2a^2}\right], \quad (2)$$

$$\widetilde{r}(x,t) = \frac{[\widetilde{U}(x,t)]_+^2}{1+\widetilde{k}\rho \int dx' [\widetilde{U}(x',t)]_+^2}, \quad (3)$$

where $\widetilde{k}$ is the strength of the global inhibition and $[X]_+ \equiv \max(X,0)$. Here we adopt a Gaussian coupling and incorporate inhibitory connections into the global inhibition.

$p(x,t)$ is the availability of neurotransmitters in neuron x. The dynamics of $p(x,t)$ is given by

$$\frac{\partial p(x,t)}{\partial t} = \frac{1-p(x,t)}{\tau_d} - \widetilde{\beta} p(x,t) \widetilde{r}(x,t), \quad (4)$$

where τ_d is the time scale of neurotransmitter recovery, which is chosen to be $\tau_d = 50\tau_s$. $\widetilde{\beta}$ is the fraction of total neurotransmitters consumed by firing per spike. This implies that when the firing rate $\widetilde{r}$ is 0, p will gradually recover to 1 and the effective connection strength will be exactly given by $J(x,x')$. However, p is less than 1 for active neurons and the connection strength is undermined by inefficient transmission. For simplicity of analysis, we introduce the rescaled variables and parameters: $U \equiv \rho J_0 \widetilde{U}$, $\beta \equiv \tau_d \widetilde{\beta}/(\rho J_0)^2$, $r \equiv (\rho J_0)^2 \widetilde{r}$, $k \equiv 8\sqrt{2\pi} a \widetilde{k}/(\rho J_0)^2$ and $I \equiv \rho J_0 \widetilde{I}$. So that we could rewrite Eqs. (1)-(4) as below.

$$\tau_s \frac{\partial U(x,t)}{\partial t} = \int_{-L/2}^{L/2} dx' \frac{1}{\sqrt{2\pi}a} e^{-\frac{(x-x')^2}{2a^2}} p(x',t) r(x',t) - U(x,t) + I(x,t), \quad (5)$$

$$\tau_d \frac{\partial p(x,t)}{\partial t} = 1 - p(x,t) - \beta p(x,t) r(x,t), \quad (6)$$

$$r(x,t) = \frac{[U(x,t)]_+^2}{1+\frac{k}{8\sqrt{2\pi}a} \int dx' [U(x',t)]_+^2}. \quad (7)$$

In the absence of external inputs ($I(x,t) = 0$), a variety of interesting behaviors have been discovered, such as the static bump, the moving bump and the silent state (Fig. 1(a)-(c), see also [16]). The static bump state, also known as a persistent spatially localized activity state [24], is of interest because it can be found in physiological recordings in the prefrontal cortex during spatial working memory tasks and other systems that encode directional or spatial information, such as head direction cells in thalamus and basal ganglia and place cells in the hippocampus. The existence and stability of the static bump state were first analyzed in detail by Amari [2], followed by various extensions. Because of the translational invariance of the neuronal coupling $J(x,x')$, the center of the static bump can be arbitrarily positioned. This is referred to as neutral stability, which leads to the naming of continuous attractor neural networks and the remarkable tracking ability of this model.

The moving bump state corresponds to traveling waves which have been extensively studied experimentally [25–27] and theoretically [28–32]. In our model, neurotransmitters are depleted at the bump's position due to the STD. Thus, the bump tends to move away to regions where neurotransmitters are more available, which is analogous to the spreading of forest fire as the fire also moves from places where trees are all burnt out, to places where fuels are abundant. This spontaneous movement is proposed to be able to compensate various kinds of delays in the neural system and therefore facilitate an accurate representation of moving stimuli [18]. However, these behaviors are found where the global inhibition k is relatively large. The parameter region where k is very small is not much explored yet.

A. Phase Diagram

The global inhibition plays an important role in shaping the bump states. Regions with low activity will be suppressed by regions with high activity through the global inhibition, thus the neuronal activity will be localized to form a state with only one bump, either moving or static. In the very weak global inhibition scenario, we expect that neural activity would be more uniform and synchronized [33]. In the uniform firing state, the firing rates of all neurons are uniform and time-independent (Fig. 1(d)).

Another possible effect of very weak global inhibition is that, neuronal activity will be relatively higher and more neurotransmitters are consumed, which induces population spikes. The neuronal activity grows up very fast due to the weak inhibition and a large amount of neurotransmitters are consumed. Then, the activity will die down because of the STD. This is called a population spike (also called ensemble synchronization) [34, 35]. After the activity dies down, neurotransmitters will gradually recover to the level that can support another population spike. These population spikes show various dynamics, including homogeneous spikes and the spike-and-anti-spike state, in the very weak global inhibition scenario (Fig. 1(e-f)).

In the homogeneous spike state, all neurons in the network are synchronized in population spikes (Fig. 1(e)). In the spike-and-anti-spike state, one spike emerges at a certain place in the network, then splits into two symmetric branches of moving bumps, which will collide with each other at the opposite side of the network and form

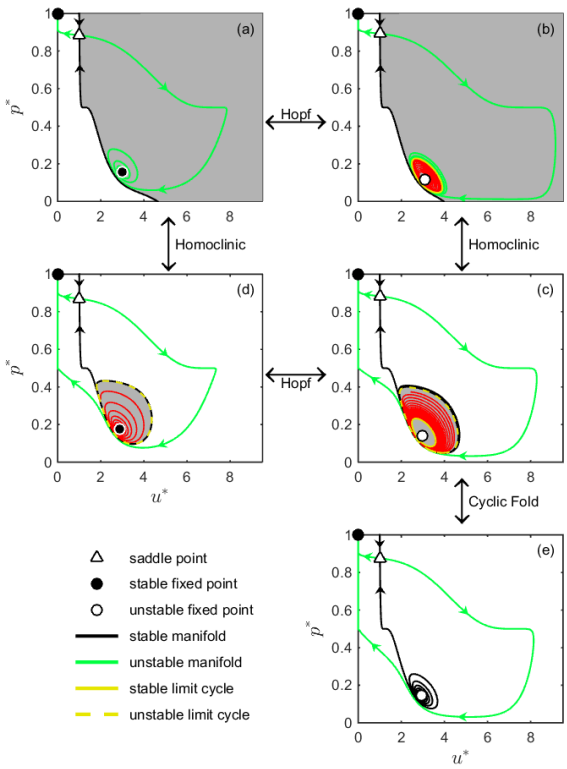

FIG. 5. (Color online) Different behaviors of simplified homogeneous dynamics. Variables are rescaled as $u^* = u^{0.3}$ and $p^* = (p-0.5)^5/0.5^4 + 0.5$ to make a readable presentation of trajectories while keeping topological equivalence. Gray area is the basin of attraction for the stable fixed point or the stable limit cycle. Some trajectories are colored red to illustrate their approach to a stable limit cycle or stable fixed point. (a) Uniform firing without an unstable limit cycle. Parameters: $k = 5\times10^{-4}$, $\beta = 0.025$. (b) Homogeneous spikes without an unstable limit cycle. Parameters: $k = 1\times10^{-4}$, $\beta = 0.023$. (c) Homogeneous spikes with an unstable limit cycle. Parameters: $k = 2.9\times10^{-4}$, $\beta = 0.0253$. (d) Uniform firing with an unstable limit cycle. Parameters: $k = 7\times10^{-4}$, $\beta = 0.0285$. (e) Silent state. Parameters: $k = 3\times10^{-4}$, $\beta = 0.027$. For (a)-(e), $a = 0.6$.

the anti-spike, and the firing activities stop. The cycle then repeats itself periodically (Fig. 1(f)).

In some parameter regions, spikes and anti-spikes can be chaotic. In the simulation, the initial condition is chosen to make spikes and anti-spikes appear at $x = 0$ and $x = \pi$, respectively. We could see the chaotic behavior by just looking at the dynamics at $x = 0$ (Fig. 2). Define $u^n_{\max}$ as the nth peak of $U(0,t)$ and $t^n_{\max}$ as the temporal interval between the nth and $(n+1)^{\text{th}}$ peaks of $U(0,t)$. By examining the relation between $u^{n+1}_{\max}$ and $u^n_{\max}$ (Fig. 3(a)), we could see it shows chaotic features. The relation between temporal intervals between spikes and the height of spikes (Fig. 3(b) and (c)) shows that the

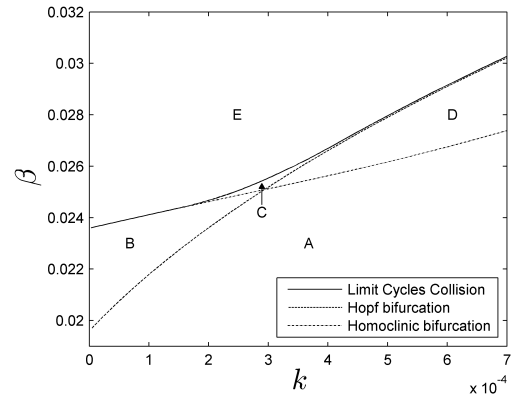

FIG. 6. Phase diagram of simplified homogeneous dynamics for interaction range $a = 0.6$. Region A, B, C, D and E correspond to behaviors in Fig. 5(a), (b), (c), (d) and (e), respectively.

height of a spike is almost linearly dependent on the resting time before that spike, rather than after that spike. Since longer resting times mean fuller recovery of neurotransmitters, the population spike following a long resting time is able to reach a greater height.

Simulations are performed to find the boundaries of these behaviors in the phase space (Fig. 4). In the phase diagram, uniform firing phase is found where k is less than 4×10^{-4} and β is less than 0.02. When k increases, the uniform firing state becomes moving bumps. This is because stronger global inhibition will suppress the homogeneity of the dynamics. When β increases, the uniform firing state becomes homogeneous spikes (dark gray area in Fig. 4(b)). The homogeneity of the dynamics is maintained, but stronger STD introduces temporal modulation. Spikes and anti-spikes (light gray area in Fig. 4(b)) are found when β is even larger. Some part of this area overlaps with moving bump region, which indicates the coexistence of the two behaviors.

B. Simplified homogeneous dynamics

In the phase diagram shown in Fig. 4(b), there is a phase called uniform firing. To study the stability of this pattern, we simplified the dynamics in Eqs. (5) and (6) to be a pair of spatially independent differential equations:

$$\tau_s \frac{\partial u(t)}{\partial t} = -u(t) + \frac{p(t)\,u(t)^2}{B} J_a, \tag{8}$$

$$\tau_d \frac{\partial p(t)}{\partial t} = 1 - p(t) - \frac{\beta p(t)\,u(t)^2}{B}. \tag{9}$$

Here, $u(t)$ represents the spatially independent $U(x,t)$. $J_a \equiv \text{erf}[L/(\sqrt{8}a)]$ and $B \equiv 1 + kL/(8\sqrt{2\pi}a)u^2$. The

nullclines for du/dt and dp/dt are

$$u = \frac{pu^2}{B} J_a,$$
$$1 - p = \frac{\beta p u^2}{B}. \tag{10}$$

Intersections between nullclines are fixed point solutions. At the intersections,

$$u = \frac{J_a \pm \sqrt{J_a^2 - 4\left(\beta + \frac{kL}{8\sqrt{2\pi}a}\right)}}{2\left(\beta + \frac{kL}{8\sqrt{2\pi}a}\right)}. \tag{11}$$

Besides fixed point solutions, limit cycles could also appear through the Hopf bifurcation or the homoclinic bifurcation [36]. In Fig. 5, there are typical phase portraits in the simplified system for different values of k and β. In Fig. 5(a), there are two stable fixed points, one representing the silent state and the other representing the uniform firing state. The stable manifold of the saddle point is the boundary separating basins of attraction of the two stable fixed points. Temporal oscillations exist in the transient state, but the firing rate is time-independent at the steady state. The fixed point for uniform firing loses its stability in Fig. 5(b), and a stable limit cycle appears around it, which demonstrates a Hopf bifurcation. The stable limit cycle corresponds to homogeneous spikes. Between Fig. 5(a) and (d), a homoclinic bifurcation occurs. The unstable manifold of the saddle point touches its stable manifold, resulting in a homoclinic orbit, which is also an unstable limit cycle encircling the basin of attraction of the uniform firing fixed point. Beyond the homoclinic bifurcation, the unstable limit cycle is no longer homoclinic and shrinks in Fig. 5(d). Although this unstable limit cycle does not affect the stability of the fixed points, it confines the basin of attraction of the uniform firing state. Between Fig. 5(b) and (c), the same homoclinic bifurcation happens and the unstable limit cycle is the basin boundary of the stable limit cycle. Between Fig. 5(c) and (d), the Hopf bifurcation same as the one between Fig. 5(a) and (b) happens. Between Fig. 5(c) and (e), the stable limit cycle and the unstable limit cycle approach each other and collide, which makes a fold bifurcation of cycles [36].

To study the stability of the above fixed point solutions, we assume that $u(t) = u_0 + u_1(t)$ and $p(t) = p_0 + p_1(t)$, where u_0 and p_0 are the fixed point solution being investigated. By linearizing Eqs. (8) and (9), we have

$$\frac{d}{dt}\begin{pmatrix} u_1 \\ p_1 \end{pmatrix} = \begin{pmatrix} \frac{2p_0u_0J_a - B}{\tau_s B} & \frac{{u_0}^2 J_a}{\tau_s B} \\ -\frac{2\beta p_0 u_0}{\tau_d B} & -\frac{B + \beta {u_0}^2}{\tau_d B} \end{pmatrix} \begin{pmatrix} u_1 \\ p_1 \end{pmatrix}. \tag{12}$$

There are two non-zero fixed point solutions to Eqs. (8) and (9): one with large u and the other with smaller u, as shown in Eq. (11) (see Appendix A). At the fixed point solution with smaller u, the determinant of the matrix in Eq. (12) is negative. Hence it is a saddle point (triangles in Fig. 5).

At the fixed point solution with larger u, the determinant is always larger than zero. The stability condition is given by the trace of the matrix. In order to have a stable fixed point solution, the trace should be less than zero. After some algebra, the phase boundary of uniform firing is given by

$$\begin{cases} k = \frac{8\sqrt{2\pi}aJ_a^2}{L}\left(\frac{\tau_s}{\tau_d}\right)^2 \frac{B-1}{(2-B)^2} \\ \beta = \frac{\tau_s J_a^2}{\tau_d}\frac{2-(1+\tau_s/\tau_d)B}{(2-B)^2} \end{cases}, \tag{13}$$

where $B > 1$. This is a parametric expression for the boundary of the Hopf bifurcation (the dashed line is Fig. 6). Other bifurcation curves in the phase diagram of this simplified system (Fig. 6) can be found using the numerical continuation package MATCONT [37]. We can see that this simplified model captures homogeneous behaviors very well. However, for inhomogeneous behaviors, we need to consider the wave stability of the fixed point solutions of Eqs. (5) and (6).

C. Wave stability of the uniform firing

To understand why moving bump disappears in such low values of inhibition and what small parameter characterizes the existence of uniform firing, we consider fluctuations with wave vector q, so that $U(x,t) = u_0 + u_1(t)e^{iqx}$ and $p(x,t) = p_0 + p_1(t)e^{iqx}$, where u_0 and p_0 are given by the steady state solution. Putting these into Eqs. (5) and (6), and keeping terms up to the first order, we have

$$\frac{d}{dt}\begin{pmatrix} u_1 \\ p_1 \end{pmatrix} = \begin{pmatrix} \frac{2p_0u_0Q - B}{\tau_s B} & \frac{{u_0}^2 Q}{\tau_s B} \\ -\frac{2\beta p_0 u_0}{\tau_d B} & -\frac{B + \beta {u_0}^2}{\tau_d B} \end{pmatrix} \begin{pmatrix} u_1 \\ p_1 \end{pmatrix}, \tag{14}$$

where $Q = \int_{-L/2}^{L/2} dx' \frac{1}{\sqrt{2\pi}a} \exp[-\frac{(x-x')^2}{2a^2} - iq(x-x')]$. Note that here we just consider wave fluctuations, thus B is not affected by the fluctuations to the first order.

To evaluate Q, we can express the integral in terms of Hermite polynomials,

$$Q = e^{-a^2q^2/2}\left[\mathrm{erf}\left(\frac{L}{\sqrt{8}a}\right) - 2\sum_{n=1}^{\infty}\frac{e^{-L^2/8a^2}}{\sqrt{\pi}n!}\left(-\frac{iqa}{\sqrt{2}}\right)^n H_{n-1}\left(\frac{L}{\sqrt{8}a}\right)\right]. \tag{15}$$

Owing to the smallness of the Gaussian factor in the higher order terms, we can approximate Q by $J_a e^{-a^2q^2/2}$, where $J_a \equiv \mathrm{erf}\left[L/(\sqrt{8}a)\right]$, or approximately 1 when $a \ll L$.

For fixed point solutions, the stability condition is the trace of the stability matrix, $T \leq 0$. Hence the phase boundary is given by $T = 2p_0u_0J_ae^{-a^2q^2/2}/B - 1 -$

$\left(1+\beta {u_0}^2/B\right)\tau_s/\tau_d = 0$. Combining with the steady state solutions, we can express the stability condition as

$$2e^{-a^2q^2/2} - 1 = \frac{\tau_s}{\tau_d}\left(1+\frac{\beta {u_0}^2}{B}\right). \tag{16}$$

Numerical solutions show that the instability comes from the long wavelength mode. For a ring model of length L, the fundamental mode has a wave number $q = 2\pi/L$. Hence for $L = 2\pi$, $q = 1$. Combining with results on the steady state solutions, the boundary of wave stability is

$$k = \frac{8\sqrt{2\pi}a}{L}\left(\frac{p_0}{1-p_0}\beta - \frac{1}{(1-p_0)^2}\beta^2\right), \tag{17}$$

where the value of p_0 on the boundary is $(2e^{-2\pi^2a^2/L^2} - 1)^{-1}\tau_s/\tau_d$. This boundary is plotted as the dot-dashed line in Fig. 4(b) and it agrees very well with the boundary between the uniform firing and the moving bump. The maximum of k on this boundary is

$$k_{\max} = \frac{2\sqrt{2\pi}J_a^2}{\left(2e^{-2\pi^2a^2/L^2}-1\right)^2}\cdot\frac{{\tau_s}^2 a}{{\tau_d}^2 L}. \tag{18}$$

This shows that the smallness of k comes from the scaling $(\tau_s/\tau_d)^2\, a/L$. On the other hand, the maximum of β on the boundary is

$$\beta_{\max} = \frac{2e^{-2\pi^2a^2/L^2} - 1 - \tau_s/\tau_d}{\left(2e^{-2\pi^2a^2/L^2}-1\right)^2}\cdot\frac{J_a^2\tau_s}{\tau_d}. \tag{19}$$

This shows that the smallness of β comes from the scaling τ_s/τ_d.

III. RESPONSES TO A SINGLE STATIC INPUT

In this section, we will discuss the network behavior in the presence of a single static input and moderate global inhibition. For the external input in Eq. (5), we adopt the form $I(x,t) = A\exp[-(x-z)^2/(2a_A^2)]$, where z is the center of that input (without loss of generality, $z = 0$ in this work), A is the strength of the input, and a_A is the width of the input. Note that the behavior of this system is controlled by three parameters, namely the strength of the global inhibition k, the strength of the STD β and the strength of the external input A. In this work, different response patterns are discussed in the parameter space spanned by these three quantities.

A. Four Basic Dynamic Response Patterns

The static bump is expected to be the simplest form of response. However, in a very large region of the parameter space, static bumps are unstable and much more interesting response patterns emerge. Among them, there are four basic dynamic patterns through which we can understand the general property of this system (Fig. 7(a)-(d)).

One response pattern is the moving bump. Moving bumps result from the mobility of the neural field enhanced by the STD. Once a bump is built, neurotrans-

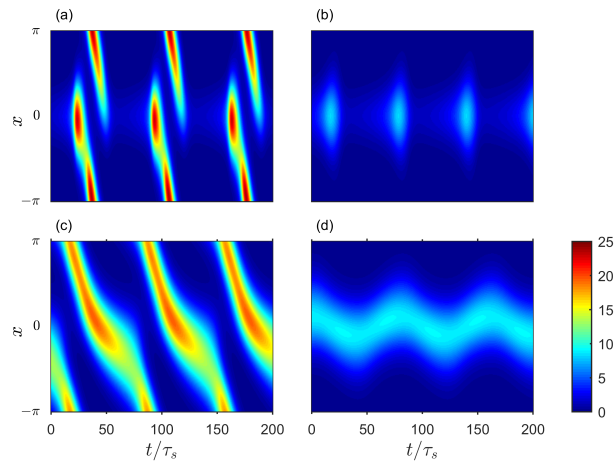

FIG. 7. (Color online) Four basic dynamic responses to a single static input in CANN with STD. The color scale shows the firing rate $r(x,t)$. (a) Emitter. Parameters: $k = 0.2$, $\beta = 0.3$. (b) Population spikes. Parameters: $k = 0.3$, $\beta = 0.4$. (c) Moving bump. Parameters: $k = 0.3$, $\beta = 0.1$. (d) Slosher. Parameters: $k = 0.5$, $\beta = 0.1$. For all (a)-(d), $A = 0.8$, $a = a_A = 48^\circ = 0.8378$.

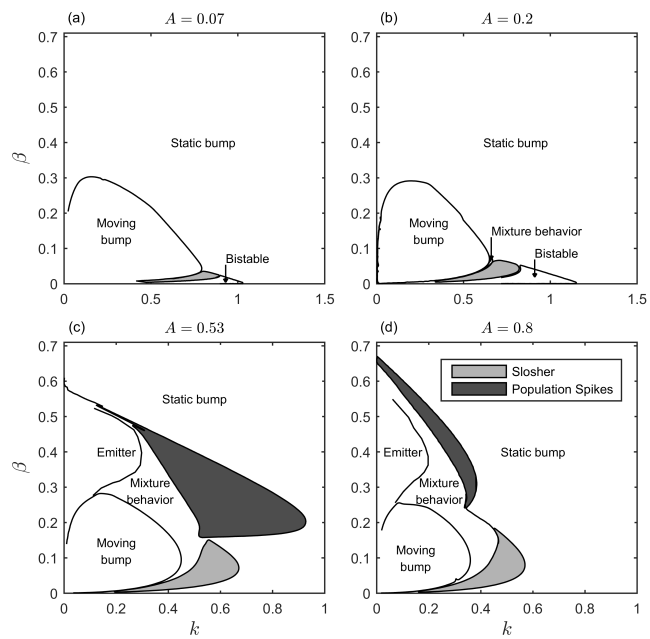

FIG. 8. Phase diagrams for the four basic responses in the space of k and β with different values of A. $a = 0.5$ and $a_A = \sqrt{2}/2$.

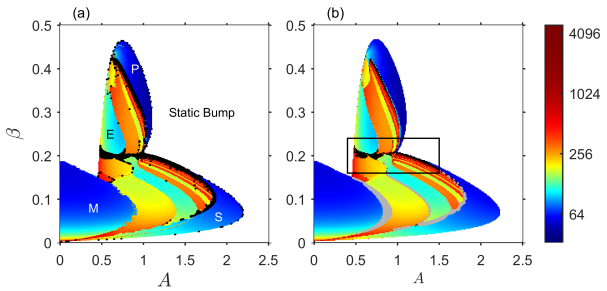

FIG. 9. (Color online) Phase diagram in the space of A and β. The color code indicates lengths of the periods in log scale. Black dots means the period of the response is too long to be detected by the program, suggesting the response is possibly chaotic. The global inhibition strength $k = 0.3$. $a = a_A = 0.8378$. (a) Full model simulation. M, E, P and S represent "moving bump", "emitter", "population spikes" and "slosher", respectively. (b) Numerical solutions of the second order Fourier series expansion. The gray regions are bistable regions where the lengths of the periods can be either of two different values. The box in (b) encircles the region where Lyapunov exponents are computed and shown in Fig. 10.

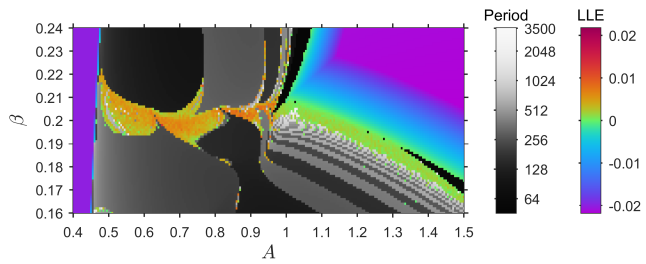

FIG. 10. (Color online) Largest Lyapunov exponents (LLE) computed on the equations of second order Fourier series expansion. Parameters are the same as those in Fig. 9. Gray scale denotes the lengths of the periods for periodic behaviors.

mitters are depleted in the bump region, leading to a tendency of the bump to move away to fresher regions. As an intrinsic behavior, the moving bump will keep its profile and its speed all the time (Fig. 1(c)). However, while the static input is imposed, the speed and profile of the bump will change when the bump crosses the input. The bump is higher and faster when approaching to the input, while weaker and slower when leaving the input, because the external input tends to attract the bump (Fig. 7(c)).

When the attraction provided by the external input is strong and the mobility enhanced by the STD is not sufficient for the bump to overcome the attraction of the input, the bump gets trapped and moves side-to-side around the external input. It is called a slosher (Fig. 7(d)) [38].

In both cases of the moving bump and the slosher, the dynamics are governed by the mobility enhanced by the STD and the attraction provided by the external input. The amplitude of the bump does not change significantly

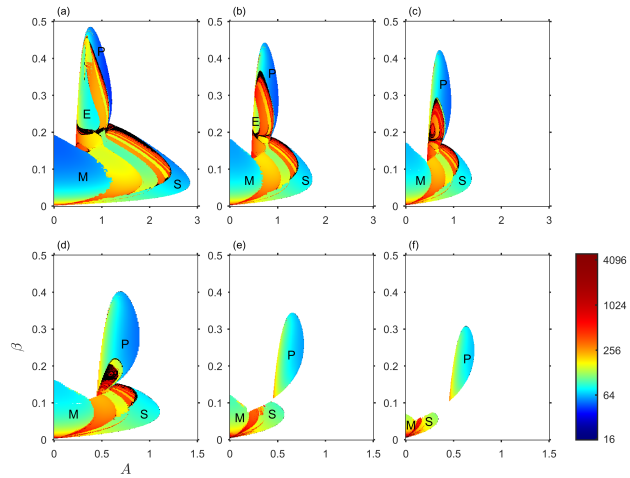

FIG. 11. (Color online) Phase diagrams in the space of A and β with different values of k. k is 0.25 in (a), 0.35 in (b), 0.40 in (c), 0.45 in (d), 0.60 in (e) and 0.70 in (f). The color code indicates the lengths of the periods in log scale. Black dots mean that the period of the response is too long to be detected by the program, suggesting the response is possibly chaotic. M, E, P and S represent "moving bump", "emitter", "population spikes" and "slosher", respectively. $a = a_A = 0.8378$.

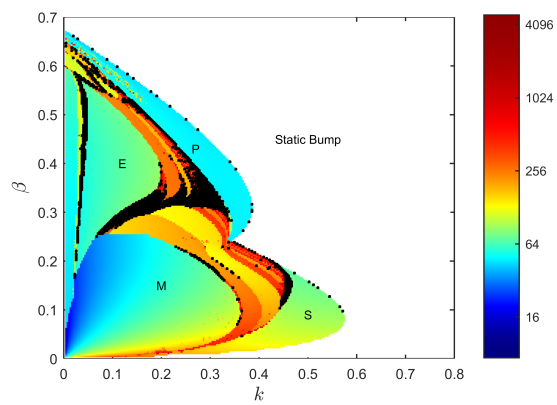

FIG. 12. (Color online) Phase diagram in the space of k and β. The color code indicates the lengths of the periods in log scale. Black dots means that the period of the response is too long to be detected by the program. Parameters: $A = 0.8$, $a = 0.5$ and $a_A = \sqrt{2}/2$.

during its movement. However, when β and A are sufficiently large, the effect of the STD is not just mobility enhancement, but also amplitude modulation. Large β and A means that the bump will consume more neurotransmitters so that it cannot maintain its amplitude all the time. The emitter (Fig. 7(a)) is an example in such case. One moving bump is emitted by the external input. After it travels around the network, the bump dies down due to the excessive consumption of neurotransmitters during traveling. Then, the network waits a while until sufficient amount of neurotransmitters is recovered to support another emission of the moving bump. When

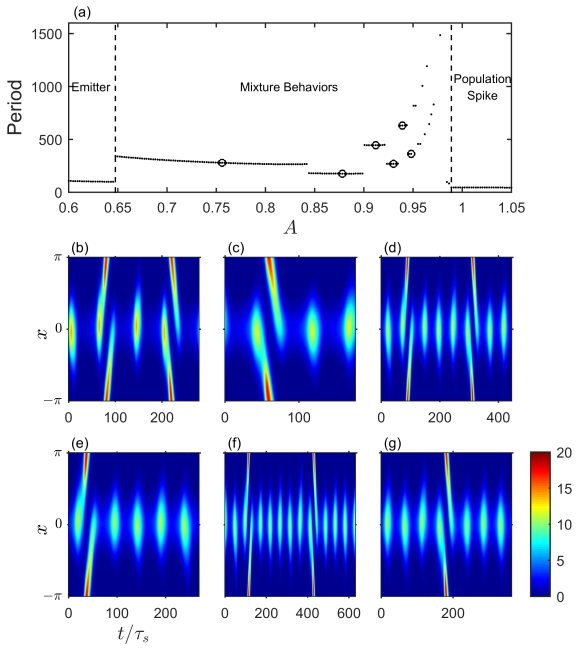

FIG. 13. (Color online) Mixtures of emitters and population spikes. (a) Periods of different responses with different input strength A. Dots are simulation results. If the period is too long to be detected, there is no dot. Six open circles are places where examples in (b)-(g) are drawn from. (b)-(g) Examples of mixture behaviors between emitters and population spikes. They correspond to the circles in (a) from left to right. Color scale indicates the firing rate $r(x,t)$. Each of (b)-(g) shows one period of the particular behavior. $k = 0.3$, $\beta = 0.3$, and $a = a_A = 0.8378$.

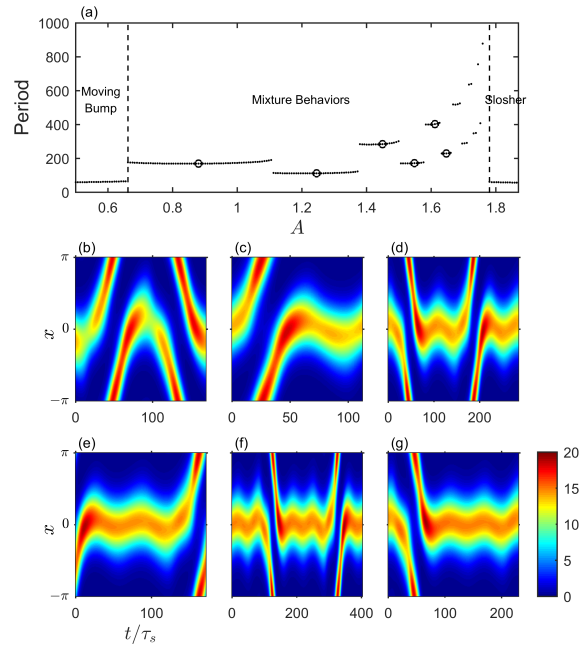

FIG. 14. (Color online) Mixtures of moving bumps and sloshers. (a) Periods of different responses with different input strength A. Dots are simulation results. If the period is too long to be detected, there is no dot. Six open circles are places where examples in (b)-(g) are drawn from. (b)-(g) Examples of mixture behaviors between moving bumps and sloshers. They correspond to the circles in (a) from left to right. Color scale indicates the firing rate $r(x,t)$. Each of (b)-(g) shows one period of the particular behavior. $k = 0.3$, $\beta = 0.13$, and $a = a_A = 0.8378$.

the external input is even stronger, we see a similar response, namely, population spikes (Fig. 7(b)), in which case a static bump, rather than a branch of moving bump, is emitted after recovery, since the external input is so strong that the bump is trapped [34, 35]. This behavior is similar to breathers [19, 39–41], except that breathers oscillate in their widths, whereas population spikes primarily oscillate in their heights.

We explore the four basic dynamic responses in the parameter space of k and β with different values of A (Fig. 8). When the input is weak (Fig. 8(a) and (b)), sloshers appear between the moving bump region and the static bump region, compared to the intrinsic behaviors in Fig. 4(a). This is because the mobility enhanced by the STD is not enough to delocalize the bump, which is attracted by the static input. When the input is strong (Fig. 8(c) and (d)), the consumption of neurotransmitters is so fast that the bump cannot keep its amplitude stable. This results in the emergence of the emitter and population spikes. We also notice that when the input is weak, there is a bistable region for static bumps. In this bistable region, there are two stable static bump solutions, corresponding to the self-sustained bump and a weaker bump that is created only when $A > 0$. A bifurcation diagram of these static bump solutions is shown in Fig. 17 and discussed in Appendix B.

B. Mixture Behaviors

In numerical solutions, we find that in a large part of the parameter space, response patterns can be none of the four basic patterns and very complex. They seem to be different mixtures of the four basic dynamic patterns. Most of these responses are periodic. The temporal duration of one period is closely related to what kind of responses are being mixed. Similar behaviors have been observed in other models of neural fields with spike frequency adaptation or short-term synaptic depression [40, 41]. However, relations between different mixture behaviors have not been systematically understood. Here, we proposed that this can be done by monitoring the period of asymptotic states. Thus, we can show how different mixture behaviors are organized in the phase diagram in the space of A and β (Figs. 9 and 11), and in the space of k and β (Fig. 12).

For the full model simulation (Fig. 9(a)), where the number of neurons is 256, Eqs. (5)-(7) are solved by using the MATLAB command ode45 and the period is determined by examining the auto-correlation function of

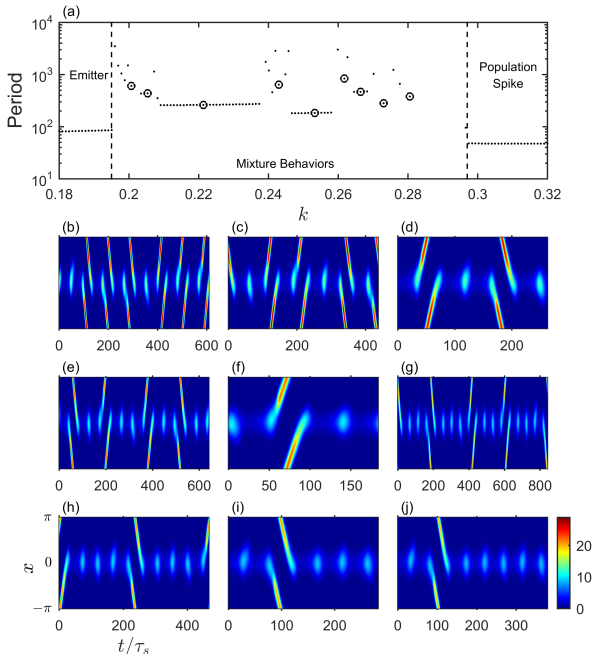

FIG. 15. (Color online) Mixtures of emitters and population spikes. (a) Periods of different responses with different global inhibition strength k. The vertical axis is in logarithmic scale. Dots are simulation results. If the period is too long to be detected, there is no dot. Nine open circles are places where examples in (b)-(j) are drawn from. (b)-(j) Examples of mixture behaviors between emitters and population spikes. They correspond to the circles in (a) from left to right. Color scale indicates the firing rate $r(x,t)$. Each of (b)-(j) shows one period of the particular behavior. $\beta = 0.36$, $A = 0.8$, $a = 0.5$ and $a_A = \sqrt{2}/2$.

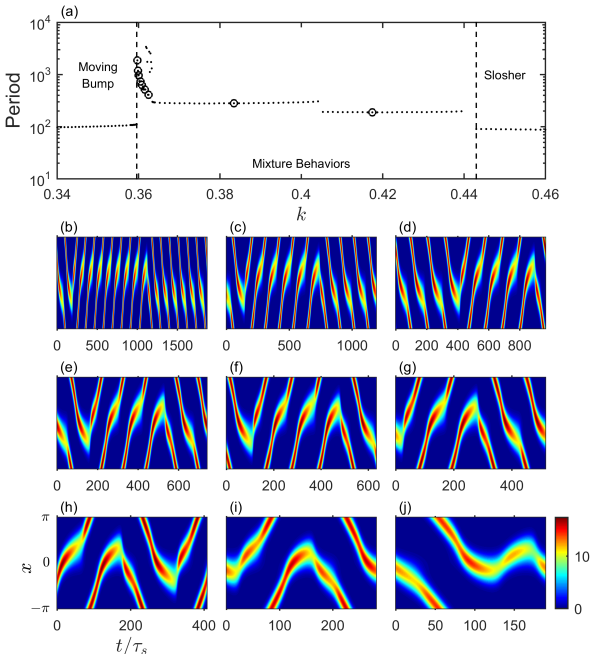

FIG. 16. (Color online) Mixtures of moving bumps and sloshers. (a) Periods of different responses with different global inhibition strength k. The vertical axis is in logarithmic scale. Dots are simulation results. If the period is too long to be detected, there is no dot. Nine open circles are places where examples in (b)-(j) are drawn from. (b)-(j) Examples of mixture behaviors between moving bumps and sloshers. They correspond to the circles in (a) from left to right. Color scale indicates the firing rate $r(x,t)$. Each of (b)-(j) shows one period of the particular behavior. $\beta = 0.1$, $A = 0.8$, $a = 0.5$ and $a_A = \sqrt{2}/2$.

asymptotic states. In Fig. 9(b), the period is determined by solving a boundary value problem of the second order Fourier series expansion (see Eq. (B3) in Appendix B) while letting A increases or decreases, using the MATLAB command bvp4c.

In the phase diagram, there are many patches within which the period of the dynamics changes continuously. However, the period jumps abruptly across boundaries of the patches. This indicates that behaviors are similar within each patch, while transitions happen across boundaries. Boundaries are relatively coarse in Fig. 9(a) due to numerical errors and the bi-stability of the dynamics, which is shown clearly in Fig. 9(b). In the gray region along phase boundaries, different dynamics can be found by starting with initial conditions from different sides of the boundaries. The four basic dynamic response patterns are located at the four disjoint regions of the phase diagram. In between them, there is a rich spectrum of different mixture behaviors. Especially, black dots, where the length of the period is too long to be well determined within a time limit, are found in the mixture behavior region, which may imply chaos. Largest Lyapunov exponents are computed using Wolf's algorithm [42, 43] in regions containing black dots (Fig. 10). Positive exponents exist extensively around $\beta = 0.2$, which clearly demonstrates the existence of chaos in this strongly coupled neural field. In the green area to the left of the sloshers region, sloshers are quasi-periodic due to the Neimark-Sacker bifurcation [36] illustrated in Fig. 17 in Appendix B. The similarity between Fig. 9(a) and (b) justifies the method of using the Fourier basis to study this system.

C. Phase Diagrams

Having explored the phase diagrams in different situations, we find that the parameter space can be separated into two parts. The upper part where β is larger consists of emitters, population spikes and their mixtures (Fig. 13 and 15). The lower part where β is smaller consists of moving bumps, sloshers and their mixtures (Fig. 14 and 16). Between these two parts around $\beta = 0.2$, responses tend to have very long period and show chaotic features. We may conclude that short-term synaptic depression have different effects depending on its strength.

Weak STD enhances the mobility of the bump without affecting the amplitude of the bump significantly, leading to bumps of relatively stable amplitude and varying posi-

tion. This is the spatial modulation effect of the STD. In Fig. 16, we see that as the external input gets stronger and stronger, the mixture behaviors tend to have less and less emitter components but more and more slosher components, from Fig. 16(b) to (g).

On the other hand, strong STD disrupts the bump in time, since neurotransmitters are depleted rapidly during the spikes. This shows the temporal modulation effect of the STD. Bumps in the time sequence generally are not the same, implying a possibility to encode different information in different emissions, an example having been discussed in detail in [20]. In Fig. 13, we see that emission of population spikes progressively dominate over emission of moving bumps as A increases from Fig. 13(b) to (g).

Varying the global inhibition at a constant external stimulus strength shows similar effects. Stronger inhibition suppresses activities in the region outside the external stimulus, therefore confines the bump or spikes to the region near the external stimulus. Hence for the case of strong STD shown in Fig. 15, the emitter components in the mixture behavior are progressively replaced by population spikes when global inhibition increases. Similarly, for the case of weak STD in Fig. 16 the moving bump components in the mixture are progressively replaced by sloshers when global inhibition increases.

IV. DISCUSSION

We have found a rich spectrum of firing patterns in CANNs with STD in the regime of weak inhibition and the regime of a single static input. CANNs with moderately strong inhibition were initially introduced to track continuous inputs using static and moving bumps. However, in the very weak global inhibition region, CANNs can no longer support bumps. Instead, the dynamics of the network show population spikes of various kinds. In particular, chaotic behavior is found in the amplitudes of the population spikes, typical of cycles of storing and releasing resources (neurotransmitters) in pulses. The smallness of STD scales as τ_s/τ_d and the smallness of the global inhibition scales as $(\tau_s/\tau_d)^2(a/L)$.

In the case of a single static input, we have found four basic patterns of dynamic responses and their mixtures. When STD is weak (lower than 0.2, roughly), it mainly provides spatial modulation, or in other words, enhances the mobility of the bump. Inputs of different strengths provide different attraction, leading to moving bumps, sloshers or mixtures of them. When STD is strong, STD provides temporal modulation along with spatial modulation. Together with the static external input, they results in emitters, population spikes, or mixtures of them. In the parameter region where STD strength is intermediate, chaotic behaviors appear. Although it is not fully understood, we believe that the involvement of both temporal and spatial modulation of STD is the major cause of complexity in that region.

Due to their richness, the firing patterns have potentials in encoding and decoding information. An example is the decoding of two inputs that fluctuate in time and overlap in the space of preferred stimuli so strongly that their time average becomes indistinguishable. Hence any time-independent decoding methods are rendered ineffective. In [20] we demonstrated that temporal modulations of the population spikes can provide a mechanism to resolve the two inputs, and produce results consistent with the resolution enhancement in transparent motion [10].

Bifurcation analysis has provided important insights into the neural field dynamics, indicating underlying mechanisms for a variety of dynamical behaviors. In [44], a similar neural field model with linear spike frequency adaptation was studied with detailed bifurcation analysis. In the presence of a simple weak input, their model also shows static bumps, moving bumps, and sloshers. The population spikes, which need a relatively strong input (Fig. 8), were not found in [44] because the inputs were relatively weak. A potential mechanism for perception switching with complex inputs mediated by sloshers was proposed. In [45], a mechanism leading to chaos was shown in effect in the single neuron model with short-term synaptic plasticity. The chaotic behavior emerges through a Shil'nikov bifurcation of homoclinic orbits. Together with our mechanism on the population level, how the short-term synaptic plasticity enhances signal processing in the neural system across multiple levels should be of interest for further studies.

Furthermore, the existence of chaotic behaviors in our network is relevant to the so-called "edge-of-chaos" region, which has been observed to coincide with best computational competence [46, 47]. Near the edge of chaos, the behavior of the network is neither dominated by the internal dynamics so as to be insensitive to external inputs, nor does it depend on the external perturbations so much as to be vulnerable to any noise. Although some argued that operating near the edge of chaos is neither a sufficient nor necessary condition for the system to achieve the best computational power [48], chaotic neural networks are still often resorted to in modeling generic cortical microcircuits [49].

Our work shows that even a recurrent network with a highly regular structure can support extremely complex dynamics and chaos, in the presence of short-term synaptic plasticity. Previous work showed that when randomly connected recurrent neural networks exhibit chaotic activities, they act as a dynamical repertoire powerful in performing a variety of complex computational tasks [50, 51] and capable of reproducing main features of certain experiments [52] through different learning rules. However, the randomness in their connectivity and the overwhelming richness of their dynamics make theoretical understanding and predictable generalization difficult [53, 54], although in some cases dynamical skeletons can be extracted to elucidate how the network achieves different functions [55]. In CANNs with STD, the edge of chaos emerges in the region where the primary effect of STD changes from spatial modulation to temporal mod-

ulation. A rich spectrum of dynamical behaviors can be readily found and understood near the edge of chaos. How to tap into the potential computational power of CANNs with STD is an interesting problem to be investigated in the future.

ACKNOWLEDGMENTS

This work is supported by the Research Grants Council of Hong Kong (grant numbers 604512, 605813 and N_HKUST606/12), National Basic Research Program of China (2014CB846101) and the National Natural Science Foundation of China (31261160495). We are grateful to Jean-Pierre Nadal and Gianluigi Mongillo for helpful discussions.

Appendix A: stability analysis of fixed points in the simplified homogeneous dynamics

The trace T and determinant D of the Jacobian matrix of Eqs. (8) and (9) are,

$$T = -1 + J_a \frac{2p_0 u_0}{B^2} - \frac{\tau_s}{\tau_d}\left(1 + \frac{\beta {u_0}^2}{B}\right), \tag{A1}$$

$$D = \frac{\tau_s (u_0 J_a - 2)}{\tau_d B}. \tag{A2}$$

For the two fixed point solutions in Eq. (11),

$$D = \pm \frac{\tau_s \sqrt{J_a^2 - 4\gamma}}{2\gamma \tau_d B}\left(J_a \pm \sqrt{J_a^2 - 4\gamma}\right), \tag{A3}$$

where $\gamma \equiv \beta + kL/(8\sqrt{2\pi}a)$ and plus signs are for the solution with larger u. D is the product of the two eigenvalues. Therefore, the fixed point with smaller u is a saddle point with $D < 0$ (triangles in Fig. 5), whereas the stability of the fixed point with larger u ($D > 0$) depends on the sign of the trace T. Combining Eq. (A1) with the expression for the nullclines in Eq. (10) and the definition for B, we can derive the parametric expression (Eq. (13)) for the boundary where $T = 0$.

Appendix B: Fourier series expansion of the CANNs model

For the CANN model Eqs. (5)-(7) and the external input $I(x,t) = A\exp[-(x-z)^2/(2a_A^2)]$, where a_A is the width of the input, we expand $U(x,t)$ and $p(x,t)$ in terms of Fourier series up to M^{th} order,

$$U(x,t) = \sum_{l=-M}^{M} u_l(t) e^{i2\pi lx/L},$$

$$p(x,t) = \sum_{l=-M}^{M} p_l(t) e^{i2\pi lx/L}, \tag{B1}$$

where,

$$u_l(t) = \frac{1}{L}\int_{-L/2}^{L/2} u(x,t) e^{-i2\pi lx/L} dx,$$

$$p_l(t) = \frac{1}{L}\int_{-L/2}^{L/2} p(x,t) e^{-i2\pi lx/L} dx. \tag{B2}$$

Therefore, the CANN model can be rewritten as,

$$\tau_s \frac{\partial u_l(t)}{\partial t} = -u_l(t) + A\frac{\sqrt{2\pi}a_A}{L} e^{-2a_A^2\pi^2 l^2/L^2} + \frac{1}{B(t)} e^{-2a^2\pi^2 l^2/L^2} \sum_{q-s+v=l} p_q(t) u_s^*(t) u_v(t),$$

$$\tau_d \frac{\partial p_l(t)}{\partial t} = \delta_{l,0} - p_l(t) - \frac{\beta}{B(t)} \sum_{q-s+v=l} p_q(t) u_s^*(t) u_v(t),$$

$$B(t) = 1 + \frac{kL}{8\sqrt{2\pi}a} \sum_{l=-M}^{M} u_l^*(t) u_l(t). \tag{B3}$$

where $\delta_{l,0}$ is equal to 1 only when $l = 0$, otherwise 0. $u_s^*(t)$ is the complex conjugate of $u_s(t)$. q, s, v are all integer indices ranging from $-M$ to M.

For $M = 0$, Eq. (B3) reduces to the simplified homogeneous dynamics in Eqs. (8) and (9). For $M = 1$, Eq. (B3) is equivalent to Eq. (14) where the wave stability is analyzed. For $M = 2$, it would be complicated to apply analytical methods. However, numerical methods are far more efficient for the Fourier series expansion up to the second order than for the full network model. Moreover, almost all features of the phase diagram of the full network model are maintained in the phase diagram of Eq. (B3) with $M = 2$ (see Fig. 9(a) and (b)).

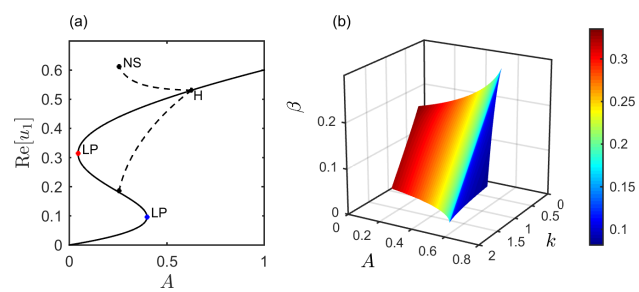

FIG. 17. (Color online) (a) The real part of the first order component u_1 of solutions of Eq. (B3) with different strengths of external inputs A. The solid line is fixed point solutions. The red dot and blue dot labeled LP (limit points) corresponds to two saddle-node bifurcations, respectively. The black dot labeled H indicates a Hopf bifurcation. The dashed lines are extrema of limit cycles. The black dot labeled NS indicates a Neimark-Sacker bifurcation. Other parameters: $k = 0.55$, $\beta = 0.08$, $a = 0.5$ and $a_A = \sqrt{2}/2$. (b) Continuation of the saddle-node bifurcation in the parameter space. The left and right surfaces corresponds to the red and blue dots in panel (a), respectively. The color scale shows the real part of the first order component u_1. The cusp bifurcation happens along the intersection of the two surfaces.

A bifurcation diagram is computed numerically using MATCONT [37] to illustrate the bistable region in Fig. 8 and the emergence of sloshers. Within the region in Fig. 17(b), there are three static bump solutions centered at $x = 0$. The lower one and higher one corresponds to the weak bump that is created only when $A > 0$ and the self-sustained bump. The middle one is a saddle point which separates basins of attraction of the other two bump solutions. The slosher appears after a Hopf bifurcation of the higher static bump state. When A decreases, it will become unstable after a Neimark-Sacker bifurcation [36], which produces quasi-periodic behaviors shown in the green area to the left of the sloshers region in Fig. 10.

[1] D. Amit, *Modeling Brain Function: The World of Attractor Neural Networks* (Cambridge University Press, 1992).
[2] S. Amari, Biological Cybernetics **27**, 77 (1977).
[3] R. Ben-Yishai, R. L. Bar-Or, and H. Sompolinsky, Proceedings of the National Academy of Sciences **92**, 3844 (1995).
[4] H. T. Blair and P. E. Sharp, Journal of Neuroscience **15**, 6260 (1995).
[5] K. Zhang, The Journal of Neuroscience **16**, 2112 (1996).
[6] J. S. Taube and R. U. Muller, Hippocampus **8**, 87 (1998).
[7] J. O'Keefe and M. L. Recce, Hippocampus **3**, 317 (1993).
[8] A. Samsonovich and B. L. McNaughton, The Journal of Neuroscience **17**, 5900 (1997).
[9] J. H. Maunsell and D. C. Van Essen, Journal of Neurophysiology **49**, 1127 (1983).
[10] S. Treue, K. Hol, and H. Rauber, Nature Neuroscience **3**, 270 (2000).
[11] A. Pouget, K. Zhang, S. Deneve, and P. E. Latham, Neural Comput. **10**, 373 (1998).
[12] S. Wu, K. Hamaguchi, and S.-I. Amari, Neural computation **20**, 994 (2008).
[13] K. Wimmer, D. Q. Nykamp, C. Constantinidis, and A. Compte, Nature Neuroscience **17**, 431 (2014).
[14] M. V. Tsodyks and H. Markram, Proceedings of the National Academy of Sciences **94**, 719 (1997).
[15] M. Tsodyks, K. Pawelzik, and H. Markram, Neural Computation **10**, 821 (1998).
[16] C. C. A. Fung, K. Y. M. Wong, H. Wang, and S. Wu, Neural Computation **24**, 1147 (2012).
[17] L. C. C. York and M. C. van Rossum, Journal of computational neuroscience **27**, 607 (2009).
[18] C. C. A. Fung, K. Y. M. Wong, and S. Wu, in *Advances in Neural Information Processing Systems 25*, edited by P. Bartlett, F. Pereira, C. Burges, L. Bottou, and K. Weinberger (2012) pp. 1097–1105.
[19] Z. P. Kilpatrick and P. C. Bressloff, Physica D: Nonlinear Phenomena **239**, 547 (2010).
[20] C. C. A. Fung, H. Wang, K. Lam, K. Y. M. Wong, and S. Wu, Frontiers in Computational Neuroscience **7**, 73 (2013).
[21] O. J. Braddick, K. A. Wishart, and W. Curran, Vision Research **42**, 1237 (2002).
[22] H. R. Wilson and J. D. Cowan, Biophysical Journal **12**, 1 (1972).
[23] C. C. A. Fung, K. Y. M. Wong, and S. Wu, Neural Computation **22**, 752 (2010).
[24] M. Camperi and X. J. Wang, Journal of Computational Neuroscience **5**, 383 (1998).
[25] R. Chervin, P. Pierce, and B. Connors, Journal of Neurophysiology **60**, 1695 (1988).
[26] D. J. Pinto, S. L. Patrick, W. C. Huang, and B. W. Connors, The Journal of Neuroscience **25**, 8131 (2005).
[27] K. A. Richardson, S. J. Schiff, and B. J. Gluckman, Physical Review Letters **94**, 028103 (2005).
[28] D. Golomb and Y. Amitai, Journal of Neurophysiology **78**, 1199 (1997).
[29] G. B. Ermentrout and D. Kleinfeld, Neuron **29**, 33 (2001).
[30] D. J. Pinto and G. B. Ermentrout, SIAM Journal on Applied Mathematics **62**, 206 (2001).
[31] P. C. Bressloff and S. E. Folias, SIAM Journal on Applied Mathematics **65**, 131 (2004).
[32] S. Coombes and M. R. Owen, SIAM Journal on Applied Dynamical Systems **3**, 574 (2004).
[33] D. Hansel, G. Mato, and C. Meunier, Neural Computation **7**, 307 (1995).
[34] A. Loebel and M. Tsodyks, Journal of Computational Neuroscience **13**, 111 (2002).
[35] S. Mark and M. Tsodyks, Frontiers in Computational Neuroscience **6**, 43 (2012).
[36] Y. A. Kuznetsov, *Elements of Applied Bifurcation Theory* (Springer-Verlag, New York, 2004).
[37] A. Dhooge, W. Govaerts, and Y. A. Kuznetsov, ACM Transactions on Mathematical Software **29**, 141 (2003).
[38] S. E. Folias, SIAM Journal on Applied Dynamical Systems **10**, 744 (2011).
[39] S. Coombes and M. Owen, Physical Review Letters **94**, 148102 (2005).
[40] S. E. Folias and P. C. Bressloff, SIAM Journal on Applied Mathematics **65**, 2067 (2005).
[41] S. E. Folias and P. C. Bressloff, SIAM Journal on Applied Dynamical Systems **3**, 378 (2004).
[42] A. Wolf, J. B. Swift, H. L. Swinney, and J. A. Vastano, Physica D: Nonlinear Phenomena **16**, 285 (1985).
[43] J. Sprott, *Chaos and Time-series Analysis* (Oxford University Press, 2003).
[44] J. Rankin, A. Meso, G. Masson, O. Faugeras, and P. Kornprobst, Journal of Computational Neuroscience **36**, 193 (2014).
[45] J. M. Cortes, M. Desroches, S. Rodrigues, R. Veltz, M. A. Muoz, and T. J. Sejnowski, Proceedings of the National Academy of Sciences **110**, 16610 (2013).
[46] C. Langton, Physica D: Nonlinear Phenomena **42**, 12 (1990).
[47] N. Bertschinger and T. Natschlger, Neural Computation **16**, 1413 (2004).
[48] R. Legenstein and W. Maass, Neural Networks **20**, 323 (2007).
[49] D. Buonomano and W. Maass, Nature Reviews Neuroscience **10**, 113 (2009).
[50] D. Sussillo and L. F. Abbott, Neuron **63**, 544 (2009).
[51] G. M. Hoerzer, R. Legenstein, and W. Maass, Cerebral Cortex **24**, 677 (2014).
[52] V. Mante, D. Sussillo, K. Shenoy, and W. Newsome,

Nature **503**, 78 (2013).
[53] W. Maass and H. Markram, Journal of Computer and System Sciences **69**, 593 (2004).
[54] H. Ju, J.-X. Xu, E. Chong, and A. M. VanDongen, Neural Networks **38**, 39 (2013).
[55] D. Sussillo, Current opinion in neurobiology **25**, 156 (2014).